

Improvement of the IRAM 30m telescope beam pattern

Carsten Kramer, Juan Peñalver, and Albert Greve[†]

August 26, 2013

Version 8.2

Abstract

The beam pattern of the IRAM 30m telescope has been derived from differential total power scans across the limb of the Moon. The 30m beam is described by the main beam and three error beams which are given by residual large-scale deformations of the primary mirror, and its frames and panels.

Total power scans across the Moon taken shortly after Full Moon at 86, 145, 210, 280 and 340 GHz in February 2010 under best late-night conditions and at optimum elevation were used to derive the beam pattern of the 30m telescope to a level of less than -30 dB and to a full width of upto $2000''$.

The analysis shows the improvement of the IRAM 30m telescope reflector from panel frame adjustments and application of ventilation and temperature control in the telescope yoke and counter weight done between 1998 and 2002. At the present low level of the error beam, transient thermal panel buckling becomes an observational effect. The paper gives an updated table of the error beam parameters and telescope efficiencies which are valid since September 2002. Recipes are given to derive the beam parameters at other frequencies. We also briefly discuss the possible degradation of the beam when observing under non-optimum conditions.

1 Introduction

A knowledge of the diffracted beam pattern and of the error beam of a radio telescope is important for calibrated measurements of point-like and extended sources. With the availability of sensitive receivers at the IRAM 30m telescope for large-scale on-the-fly mapping of Galactic sources or external galaxies, the knowledge of the beam pattern is in the focus of interest. The evaluation of the beam pattern is of particular importance for observations at 1 and 0.8 mm wavelength where the fraction of power obtained through the error beams is significant. We reported in 1998 on the beam pattern of the IRAM 30m telescope (Greve et al. 1998a, Paper I) and provided a table of error beam parameters for use since July 1997 (Table 1, Paper I). Between 1998 and 2002, the telescope has been improved by reflector panel frame adjustments and by installation of ventilation and temperature control in the telescope yoke and counter weight (Penalver et al. 2002, Greve et al. 2005). As derived from holography measurements, the adjustment has improved the surface rms-value from $\sigma \sim 65 \mu\text{m}$ to $\sigma \sim 50 \mu\text{m}$. The end of operation of the geostationary satellite ITALSAT has terminated holography measurements of the 30m reflector in 2001. A new satellite, ALPHASAT, has been launched on 25-July-2013. Its Q/V band payload includes a 39 GHz beacon which we plan to use for holography in the coming years.

The IRAM 30m telescope beam pattern can be described by the main beam plus three error beams with Gaussian profiles, power amplitudes $a_{e,i}$ and half power beam widths $\theta_{e,i}$, $i = 1, 2, 3$. Following Paper I, the 1st error beam is mainly due to large scale transient reflector surface deformations, of which astigmatism is the major component as a Zernike polynomial analysis indicates (Greve et al. 2005). The 2nd error beam is caused by misalignment of the panel frames. Its power can in principle be reduced by adjusting the frames. The 3rd error beam is caused by small scale surface errors of the individual panels. These errors are due to the fabrication and may be irregularities of the reflecting aluminium surface or inhomogeneities of the thin layer

of paint on top of the panels. As the panels cannot be adjusted relative to the frames, these errors cannot be corrected. The panel errors produce the broadest error beam.

The application of ventilation and temperature control of the yoke and counter weight has reduced the transient reflector astigmatism. In addition, the last panel frame adjustment have improved the surface precision by $\Delta\sigma \sim 15 \mu\text{m}$. Working with a reflector of this precision it was recognized that the surface shows transient thermal panel buckling (Greve & Morris 2005) which appears as a transient reduction of the main beam efficiency and a low power diffraction ring of wavelength dependent radius. Here, we show that these improvements are noticeable in lunar scans and update the parameters of the beam pattern published in 1998 (Paper 1).

An established method to obtain the beam pattern is based on total power scans across the limb of the Moon and subsequent differentiation of the Moon scans. A differentiated Moon scan is not exactly the actual beam pattern; we call the differentiated Moon scan “**composite profile**” (see also Sugimoto et al. 2004, 2010). The composite profiles must reach a level of -30 dB in order to obtain useful information of the extended error beam. The parameters describing the error beams are obtained by iterative comparison of measured composite profiles with calculated composite profiles. This method has been used in the past in a 86 GHz to 350 GHz study of the IRAM 30m telescope (Paper I), a 800 GHz study of the ASTE 10m telescope (Sugimoto et al. 2004), a 460 and 800 GHz study of the APEX 12m telescope (Güsten et al. 2006), and a 41 GHz study of the GBT 100m telescope (Nikolic et al. 2006).

2 The Method

We have shown in Paper I that the beam pattern can be obtained from a total power scan across the limb of the Moon, subsequent differentiation of this scan, and comparison with a differentiated calculated Moon limb scan. The beam pattern consists of the diffraction beam and the Gaussian error beams. For the brightness distribution of the Moon see e.g. Krotkov & Troitskii (1964). The scans are preferably made at Full Moon (night time) and New Moon (day time) because the lunar brightness distribution is then symmetric. The actual beam pattern is obtained in an iterative way, starting from an estimated initial beam pattern, comparison of the measured composite profiles and the calculated composite profile, and changing the error beam amplitudes and full widths at half maximum (FWHM), until a best fit is obtained. Below we show that the widths of the second and third errorbeam derived from the lunar scans compare well with the widths expected from the sizes of the frames and panels.

3 Measurements of 2-Feb-2010

Since the publication of Paper I, we have made several Moon limb scans, though not always under optimal atmospheric conditions and low residual thermal effects of the telescope structure. Good quality data were for example obtained 2003, 8 Oct (A.Greve, priv. comm.). Here, we present scans taken under exceptionally good conditions on 2010, 2 February. These data were taken at 86, 145, 210, 280 and 340 GHz in the second half of the night at UT between 2 and 5, 69 hours after Full Moon. The Moon elevation was between 49° and 51° , i.e. at the elevation when homology deformation of the reflector are minimal (Greve et al. 1998b, Penalver 2012). Pointing and focus were checked and corrected by observations of a nearby strong point source. The lunar data were calibrated using the standard hot/cold/sky “chopperwheel” method at 4° distance from the Moon. The

amount of atmospheric precipitable water vapor (pwv) was about 1mm (zenith opacities: 0.03 at 86 GHz, 0.04 at 145 GHz, 0.09 at 210 GHz, 0.08 at 280 GHz and 0.25 at 340 GHz).

The cross scans on the Moon have been done on-the-fly in total power mode with scan lengths of 3900'' across the Moon of $\sim 1800''$ diameter. The data sample rate was 100 msec, and the time per scan 130 s, resulting in a pixel separation of 3'' on the sky. The EMIR frontend was used in the following combinations: E0(86)&E2(210), E1(145)&E3(280) and E1(145)&E3(340). The narrow band continuum (nbc) backend with 1 GHz bandwidth was used for these observations¹. Three or four cross scans were done with each receiver combination. No baselines were subtracted from these data.

The profile of a cross scan on the Moon at 340 GHz (Fig. 1) shows the convolution of the lunar disk with the beam pattern. The deviation of the profile from the intrinsically sharp lunar edge is due to the finite size of the beam pattern. To determine the composite profile, only the profile at negative offsets in Azimuth and Elevation was used, as the profile at positive offsets are less well defined about 3 days after full moon.

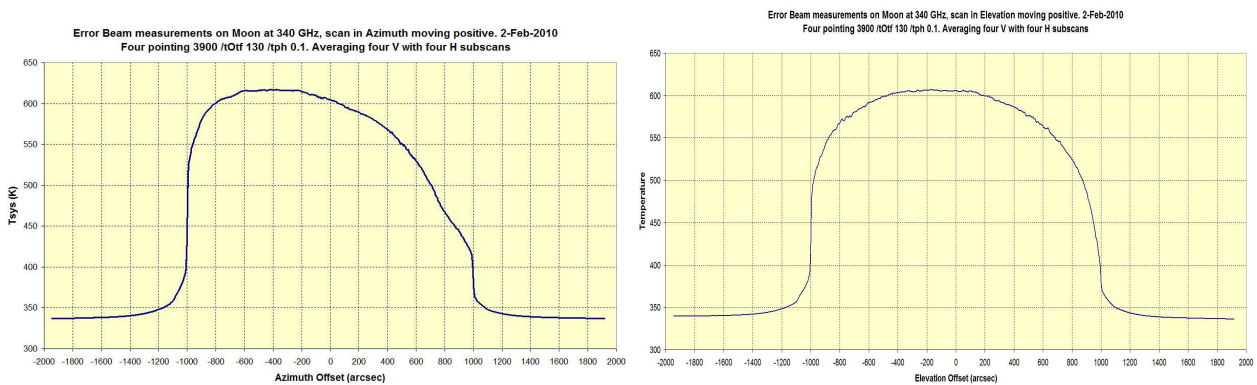


Figure 1: Scan of the Moon at 340 GHz in Azimuth (Left) and Elevation (Right).

4 Data Reduction

The data of the two polarisations were averaged. Only the subscans with positive scanning velocity have been considered to avoid any possible disagreement with the position of subscans with a negative velocity.

The observed lunar scans were differentiated in scan direction to obtain the composite profiles². The composite beam was first obtained independently for azimuth and elevation. These were then averaged, assuming that the beam pattern is axial-symmetric.

Next, synthetic composite beams were calculated from the convolution of a given beam pattern with the brightness distribution of the Moon followed by differentiation. Here, we assumed that the lunar disk is circular and of constant temperature. The synthetic beam pattern consists of the main beam and three error beams, as described in Paper I. In addition, a term describing the panel buckling has been introduced.

The synthetic composite beams were fitted by hand to the observed composite profiles, by varying the widths and amplitudes of the three error beams and the value of the buckling parameter.³

¹In February 2010, the new broad band continuum backend bbc was not yet available.

²For this, the program diff has been used.

³For this, the program prob.f was used, created from merging the original programs pro86b.f, pro150b.f, pro230b.f, pro280b.f, pro350b.f for individual frequencies of A. Greve.

	Main Beam	1. Error Beam	2. Error Beam	3. Error Beam	Buckling
86 GHz, 3.49 mm					1.5
Beam Width θ	29''	0	550''	2000''	
Correlation Length S			1.58 m	0.44 m	
Power Amplitude a	1	0	0.000220	0.000015	
Int. rel. power P	0.87	0	0.07	0.06	
145 GHz, 2.07 mm					1.2
Beam Width	16''	85''	350''	1200''	
Correlation Length		5.6 m	1.37 m	0.40 m	
Power Amplitude	1	0.000800	0.000250	0.000016	
Int. rel. power	0.81	0.02	0.10	0.07	
210 GHz, 1.43 mm					1.0
Beam Width	11''	65''	250''	860''	
Correlation Length		5.1 m	1.32 m	0.38 m	
Power Amplitude	1	0.001900	0.000350	0.000022	
Int. rel. power	0.72	0.05	0.13	0.10	
280 GHz, 1.07 mm					2.0
Beam Width	8.4''	50''	175''	620''	
Correlation Length		5.0 m	1.44 m	0.41 m	
Power Amplitude	1	0.002000	0.000500	0.000055	
Int. rel. power	0.63	0.04	0.14	0.19	
340 GHz, 0.881 mm					1.0
Beam Width	7.5''	35''	150''	510''	
Correlation Length		6.4 m	1.50 m	0.44 m	
Power Amplitude	1	0.003500	0.000800	0.000085	
Int. rel. power	0.56	0.04	0.18	0.22	

Table 1: Error beam parameters fitted to the composite beams of lunar scans done on 2-February-2010, and properties of the main beam. For each of the four beams, we list its Gaussian full widths at half maximum (FWHM) θ_i , corresponding correlation length S_i (see text), amplitude a_i , and integrated relative power P_i (cf. Eq. 1, Fig. 3). The best-fitting buckling parameter is listed in column 6.

5 Results

Figure 2 shows the observed composite beams together with the best fitting synthetic composite beams. For all five frequencies, the measurements are reliable to a level of better than -30 dB, i.e. $\sim 0.1\%$ of the peak intensity. Table 1 lists the beam parameters. The half power beamwidths of the main beam (HPBW), θ_0 , were derived independently from observations of planets smaller than the beam. The integrated relative power P_i of each beam listed in this table is normalized to the total power of all beams:

$$P_i = a_i \theta_i^2 / \sum_{i=0,3} a_i \theta_i^2. \quad (1)$$

Note that P_0 is larger than the main beam efficiency, B_{eff} (see below), due to the different normalization

Frequency GHz	B_{eff}	P'_1	P'_2	P'_3	$\sum P'$	F_{eff}	η_{fss}
86	81	0	7	6	12	95	2
115	78	1	8	6	14	94	2
145	74	2	9	6	17	93	2
210	63	4	11	9	24	94	6
230	59	4	11	11	25	92	8
280	49	3	11	15	29	87	9
340	35	2	11	14	28	81	19
345	34	2	11	14	28	80	18

Table 2: Present-day telescope efficiencies in percent. Main beam efficiencies B_{eff} were derived from observations of Uranus and Mars. The error beam efficiencies P'_i equal P_i scaled by B_{eff}/P_0 to correct for the different normalizations. Forward efficiencies F_{eff} were derived from skydips. The forward spillover and scattering efficiency, η_{fss} , is the difference between the forward efficiency and the sum of the efficiencies of the main beam plus error beams, i.e. $\eta_{\text{fss}} = F_{\text{eff}} - (B_{\text{eff}} + \sum P')$. The rearward spillover and scattering efficiency, η_{rss} (not listed), equals $1 - F_{\text{eff}}$. Telescope efficiencies at other frequencies than those observed on 2-Feb-2010 are derived from linear inter- or extrapolation (cf. Figure 4).

as explained in the following: The main beam efficiency is the power detected by the main beam relative to the power integrated over 4π , $\Omega_{4\pi}$. In other words, the sum of the power integrated over the main beam and the three error beams is smaller than $\Omega_{4\pi}$ as the latter includes also the forward and rearward spillover and scattering efficiencies, η_{fss} and η_{rss} (see Table 2).

The full widths at half maximum, θ , of the main beam and the three error beams (Table 1) are inversely proportional to the observing frequency as Figure 6 shows, i.e. the beam widths multiplied by the frequency are constant with frequency:

$$\theta['] \times \nu[\text{GHz}] = k \quad (2)$$

Beam	k
Main beam	$(24 \pm 1) 10^2$
1. Errorbeam	$(13 \pm 1) 10^3$
2. Errorbeam	$(50 \pm 2) 10^3$
3. Errorbeam	$(175 \pm 3) 10^3$

Table 3: Derived, averaged values of k .

The frequency averaged values of k are given in Table 3. Constant values are expected for a constant illumination taper with frequency and shows that the widths of the error beams are defined by correlation lengths S which are given by the structure of the main dish: $\theta = k' \lambda/S$ with k' determined from the measured HPBW θ_0 of the main beam: $\theta_0 = k' \lambda/(30 \text{ m})$. The correlation lengths of the errorbeams are listed in Table 1.

Figure 3 shows the integrated relative power P_i of the error beams, comparing the present values measured in 2010 with those of 1998 listed in Table 2 of Paper I.

Main Beam: The relative power received in the main beam has significantly increased over the entire frequency range relative to the values of 1998 (Fig. 3) while the power received through the 1st and 3rd errorbeams was reduced. The improvement of the power received through the main beam is also seen in the plot of the main beam efficiencies shown in Figure 4. For example, the main beam efficiency at 230 GHz improved from 42% to 59%. This improvement has been known for several years as documented on the corresponding IRAM web page⁴ and e.g. in the EMIR commissioning report. What is new here, is the accurate description of the corresponding reductions of the power detected through the 30m errorbeams.

First Error Beam: The 1st error beam is caused by large scale deformations of the entire dish which may be transient (Paper I). During the years 1997 to 2002, the antenna temperature control has been improved and we therefore expect that these large scale deformations are reduced in amplitude since then. The size or typical correlation lengths of these deformations is not well defined and depends on the details of the temperature regulation. In Paper I, we found typical correlation lengths of this error beam of 2.5 to 3.5 m, while here we find an average correlation length, independent of the frequency, of $5.8\text{ m} \pm 0.5\text{ m}$, corresponding to the size of about 8 frames.

Back in 1997, the power detected within this error beam varied significantly from one observation to the next, showing that this error beam is of transient nature, and reached up to 25% at the highest frequency in extreme cases. In contrast, the new observations of 2010 show that the relative power of the 1st error beam is now less than 5% at all frequencies.

Second Error Beam: The 2nd error beam is caused by frame misalignment. Holography sessions and subsequent adjustments of the frames have between 1997 and 2002 improved the overall surface accuracy of the primary. It is therefore expected that the power received through this error beam has been reduced, while its widths are not expected to change as they are determined by the typical correlation lengths of the frames (Paper I). Table 1 shows that the average correlation length corresponding to the fitted widths of the error beams is $1.49\text{ m} \pm 0.06\text{ m}$, which is indeed consistent with the values found in Paper I where we showed that the weighted distance between the centers of adjacent frames give correlation lengths of 1.5 m to 2.0 m. As each frame holds two panels, the correlation lengths also corresponds to the typical diameter of the 420 panels of the 30m telescope.

The relative power received through the 2nd error beam have hardly changed between 1998 and 2010, as Figure 3 shows.

Third Error Beam: The 3rd error beam is caused by panel deformations of typical correlation lengths 0.3 m-0.5 m (Paper I). As the panels cannot be adjusted relative to the frames, we expect that neither the width of this error beam at a given frequency, nor the received power, changes with time. Indeed, the size of this error beam at a given frequency, and the resulting average correlation length of the 3rd error beam of $0.43\text{ m} \pm 0.01\text{ m}$ (Table 1), are in accordance with Paper I.

⁴<http://www.iram.es/IRAMES/mainWiki/Iram30mEfficiencies>

The relative power received with the 3rd error beam has decreased significantly relative to 1998. We note however that the data presented in Paper I were less deep than the present data. This affects in particular the determination of the properties of the 3rd wide error beam. While the relative power does increase with frequency (Table 1) from 6% at 86 GHz to 20% at 350 GHz these power levels are more than 10% lower than those found in 1998.

Panel Buckling: The composite beam profiles shown in Figure 2 reveal diffraction rings at all frequencies. The diffraction ring is found at $\theta_d \sim 200''$ at 145 GHz, $\sim 150''$ at 210 GHz, $\sim 100''$ at 280 GHz, and $\sim 80''$ at 340 GHz. These rings have an amplitude of $\sim 2 - 3$ dB. They are not part of the diffraction rings of the Airy pattern of the primary 30m dish (cf. Fig. 5) but rather caused by thermal panel frame buckling, which acts like a grating (Greve & Morris 2005; for the Planck satellite see Nielsen 2005). The position of the rings follows the grating relation $\theta_d = n\lambda/d$ with n the order of the diffraction and d the spacing of the grating. From the observed values of θ_d we derive $d \sim 2$ m which is the dimension of a panel frame. These diffraction rings have hardly been seen earlier in total power scans, as is clearly shown in Figure 2 comparing the best fitting synthetic composite beams of 1998 with those measured 2010. The 2nd order diffraction rings are below the level of sensitivity. The thermal panel frame buckling has been seen in holography measurements which are made with a significantly higher signal to noise ratio than the composite profiles. The panel buckling is caused by a panel frame buckling due to a temperature gradient in the frames (Plathner 1997). Between day and night time, the temperature gradient in the frames and hence also the buckling apparently reverses direction. The maximum of the buckling is $\sim 30 \mu\text{m}$ to $50 \mu\text{m}$ which results in a quasi rms value (Greve 1980) of $\sigma_B \sim 10 \mu\text{m}$ to $15 \mu\text{m}$ (Greve & Morris 2005). The transient value σ_B can be quadratically added to the value of Sigma of the total surface error: $\sigma \sim \sqrt{(\sigma_T^2 + \sigma_a^2)}$ with the quasi-rms value of the large surface-scale surface deviations σ_T (Greve 1980) and the misalignment and panel surface error σ_a .

Figure 5 shows the best fitting beam profile at 280 GHz (i.e. not the composite beam) together with the underlying error beams, to give an example. The effect of the buckling on the beam shape is described by additional diffraction rings (cf. Greve et al. 2010). Here, these rings are introduced using a simplified model, i.e. by multiplying the composite profile with a scaling factor (given in Table 1) over a small range of angular offsets predicted from diffraction (cf. Greve et al. 2010).

6 Telescope Efficiencies

In Table 2 and Figure 4 we present telescope efficiencies, combining the results of the present error beam analysis with the observed main beam efficiencies, B_{eff} , and forward efficiencies, F_{eff} . Main beam efficiencies were derived from aperture efficiencies measured on Uranus and Mars, while the forward efficiencies were derived from skydips taken under good weather conditions (cf. IRAM web page)).

The data show again the little power left-over in the 1st error beam. They also show the power left in the forward spillover and scattering efficiency, η_{fss} , which includes the power in the diffraction rings caused by panel buckling. This efficiency contains less than 10% of the total power for frequencies below 280 GHz, and 20% at 340 GHz.

7 Non-optimum conditions

Above, we describe the beam shape and the beam efficiencies measured under optimum conditions, i.e. at an elevation of $\sim 50^\circ$ and during very stable weather conditions during the second half of the night. Also, wobbler switched planetary observations to measure the beam efficiencies were conducted with small throws. Here, we briefly describe the possible degradation of the beam of the 30m telescope during observations under non-optimum conditions.

We expect that a degradation of the beam shows-up in a reduction of the aperture efficiency as measured on point sources. There are at least three cases: (1) variation of the gain with elevation, (2) variation of the gain with wobbler throw, and (3) degradation of the beam during day time and clear sky when the sun partially warms the primary, which may lead to deformation of the primary. We assume here that the telescope is well pointed and focussed, and that the wind load is low.

1. The variation of the aperture efficiency with elevation, the gain-elevation curve, was described by Greve et al. (1998b) and has recently been re-observed and characterized by Penalver (2012). Independent of observing frequency, the gain-elevation curve peaks at $\sim 50^\circ$. The drop with higher and lower elevations is steepest for the highest frequencies. While the gain-elevation curve hardly show any variation at 86 GHz, the aperture efficiencies measured e.g. at 210 GHz show a relative drop by 20% at 20° and 80° elevation. At 340 GHz, the aperture efficiencies show a drop by 45%, at 20° and 80° elevation. For point sources or sources not much larger than the main beam, the observed variation of the aperture efficiencies can be used to correct their fluxes.

The report of Penalver (2012) is available on the IRAM web pages⁵ where we also offer a CLASS script which allows to correct antenna temperatures measured on point sources for this effect.

The change of beam pattern with elevation expected from models is described in Greve et al. (1998b, G98b). It loses its near axial-symmetry. We expect that the drop of aperture efficiency with elevation leads to large-scale surface errors and hence to an increase in the power detected by the first errorbeam (cf. modelled beam maps at 230 GHz for different elevations shown in Figure 2 of G98b). The gain-elevation correction to applied to observed data depends on the source size. For extended sources of about 5 times the size of the HPBW the effect is reduced to only about 30% and the effect disappears for sources ~ 8 times the HPBW (cf. Fig. 3 in G98b). Beam maps using sensitive continuum cameras may be possible in the future.

2. The telescope gain also varies with increasing tilt of the subreflector when conducting wobbler switched observations. With increasing throw, the aperture efficiency drops. Greve et al. (1996) show that also this degradation is worse for the highest frequencies. At 230 GHz, the observed and modelled drop is almost 20% for a throw of $\pm 110''$.
3. The illumination of the dish by the sun may also degrade the beam shape and beam efficiencies. As science observations are done under these conditions, observers need to know the actual efficiencies to accurately calibrate their data. We have started to collect beam efficiencies taken under varying day/night conditions.

⁵<http://www.iram.es/IRAMES/mainWiki/Iram30mEfficiencies>

8 Acknowledgements

The authors thank Jerome Pety and Karl Schuster for useful discussions and comments. This report would not have been possible in this form and at this time without the countless contributions over many years from Albert Greve who passed away on 13 June 2011.

9 References

- Greve et al. 1980, Appl. Optics 19, 2948
- **Near-focus active optics: An inexpensive method to improve millimeter-wavelength radio telescopes**
A. Greve, J.W.M. Baars, J. Penalver, B. LeFloch, 1996, Radio Science, 31, 5, 1053
- **The beam pattern of the IRAM 30m telescope**
A. Greve, C. Kramer, W. Wild, 1998a, A&ASS, 133, 271 (Paper I)
- **The gain-elevation correction of the IRAM 30m telescope**
A. Greve, R. Neri, A. Sievers, 1998b, A&ASS, 132, 413
- **Improvement of the IRAM 30m millimeter wavelength radio telescope from temperature measurements and finite element calculations**
A. Greve, M. Bremer, J. Penalver, P. Raffin, D. Morris, D. Broguire, 2005, IEEE Trans. Ant. Propagation, 53, 2
- **Repetitive Radio Reflector Surface Deformations**
A. Greve & D. Morris 2005, IEEE Trans. Ant. Propagat. AP-53, 2123
- **The beam pattern of reflector antennas with buckled rectangular panels**
A. Greve, D. Morris, J. Penalver, C. Thum, M. Bremer, 2010, IEEE Transactions on Antennas and Propagation, 58, 3, 959
- **The Atacama Pathfinder EXperiment (APEX) - a new submillimeter facility for southern skies**
R. Güsten, L.A. Nyman, P. Schilke et al. 2006, A&A, 454, 2, 13
- **Improvement of the IRAM 30-m Telescope From Temperature Measurements and Finite-Element Calculations**
A. Greve, M. Bremer, J. Penalver, P. Rafin, D. Morris, 2005, IEEE Transactions on Antennas and Propagation, 53, 2, 851
- V.D. Krotikov, V.S. Troitskii 1964, Soviet Physics Uspekhi 6, 841
- P.H. Nielsen 2005, 28th ESA Antenna Workshop on Space Antennas and Technologies, ESTEC, Noordwijk, The Netherlands, 627
- B. Nikolic, D.S. Balsler, R.M. Prestage 2006, GBT PTCS Project Note 51.1, NRAO, USA
- J. Penalver, A. Greve, M. Bremer 2002, IRAM Newsletter 54, 8

- **New measurements of the gain-elevation curves of the IRAM 30m telescope,**
Penalver 2012, IRAM Internal Report (available on the IRAM web)
- D. Plathner 1997, IRAM Working Report 244, IRAM, Grenoble
- **Cartridge-Type 800 GHz Receiver for the Atacama Submillimeter Telescope Experiment (ASTE)**
M. Sugimoto, Y. Sekimoto, K. Tetamatsu et al. 2004, PASJ, 56, 1115
- **Sensitivity Analysis of Optical Systems in Radio Telescopes**
M. Sugimoto, S. Iguchi, J. Inatani et al. 2010, PASJ, 62, 39

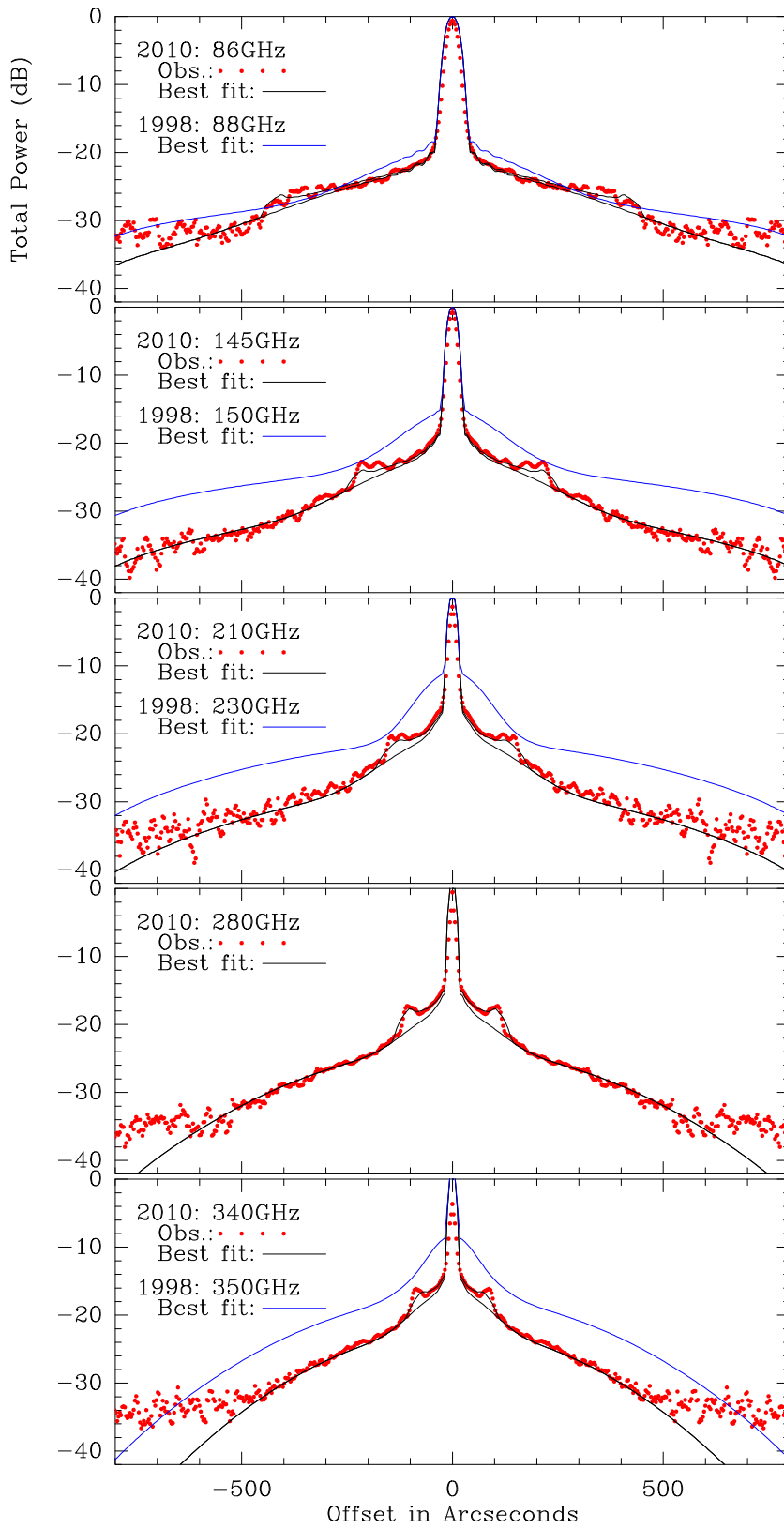


Figure 2: Composite beams observed in 2010 (red dots) together with best fitting beam model with and without panel buckling included (black curves), and the best fitting model of the data presented in Greve et al. (1998a; Paper I; blue curves). There were no data taken at 280 GHz for Paper I.

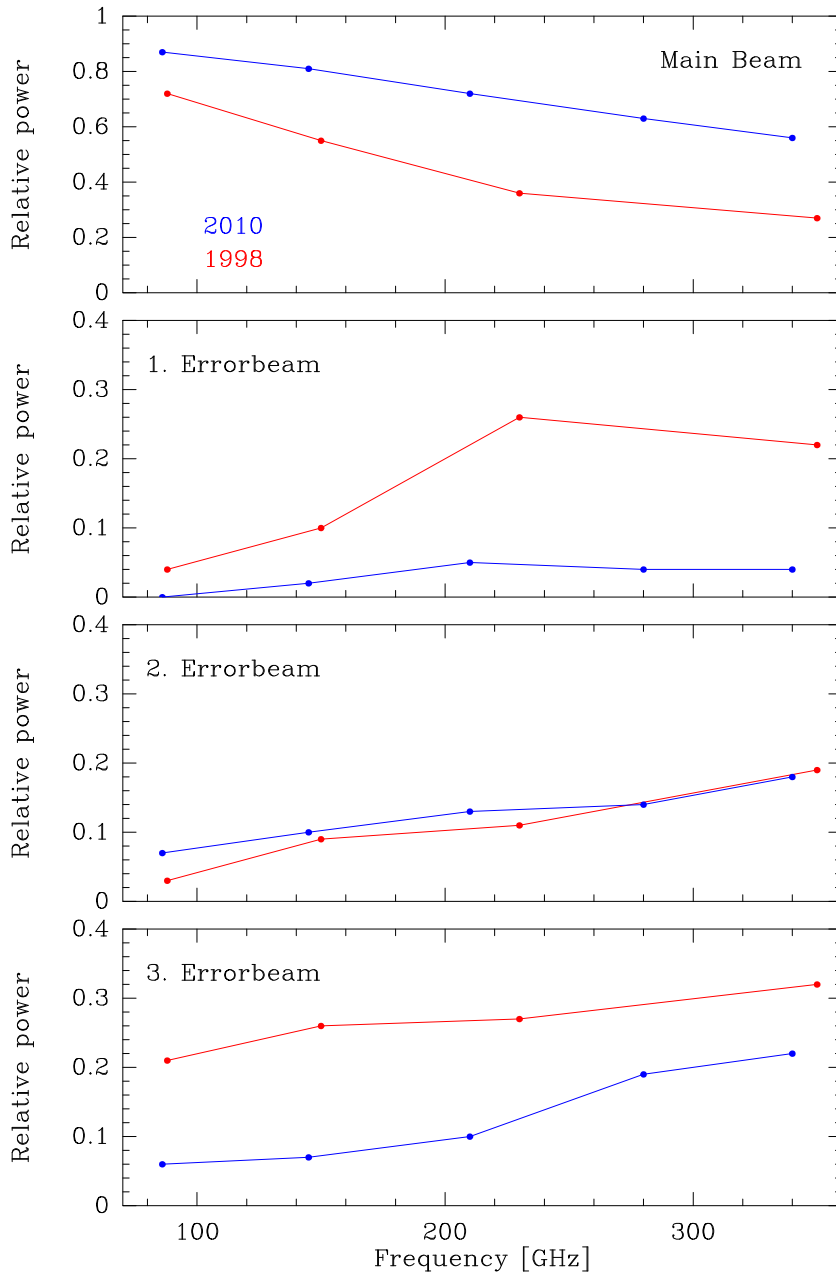


Figure 3: Integrated relative power of the main beam and of the three error beams in 1998 and now.

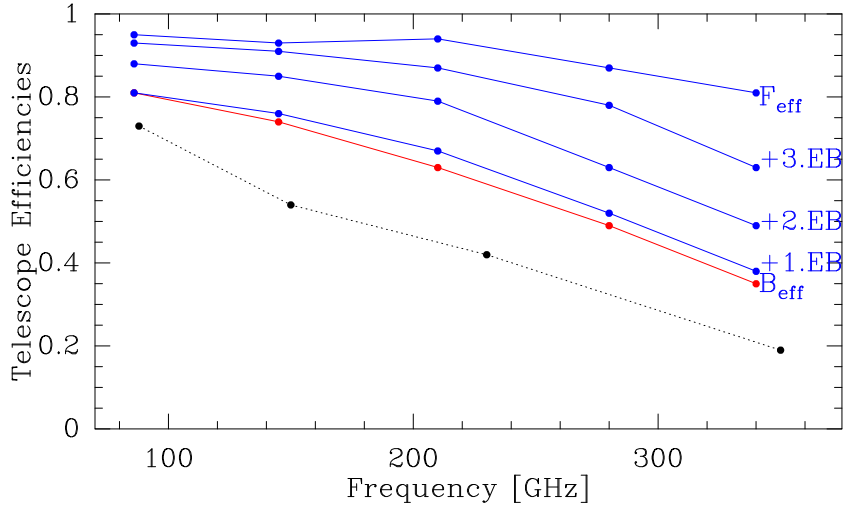


Figure 4: Telescope efficiencies (cf. Table 2). Main beam efficiencies were derived from observations of primary calibrators Uranus or Mars. The forward efficiencies were derived from skydips. The properties of the three errorbeams are based on the lunar data taken in 2010 which are presented here. The dashed line shows the main beam efficiencies in 1998 (Paper I).

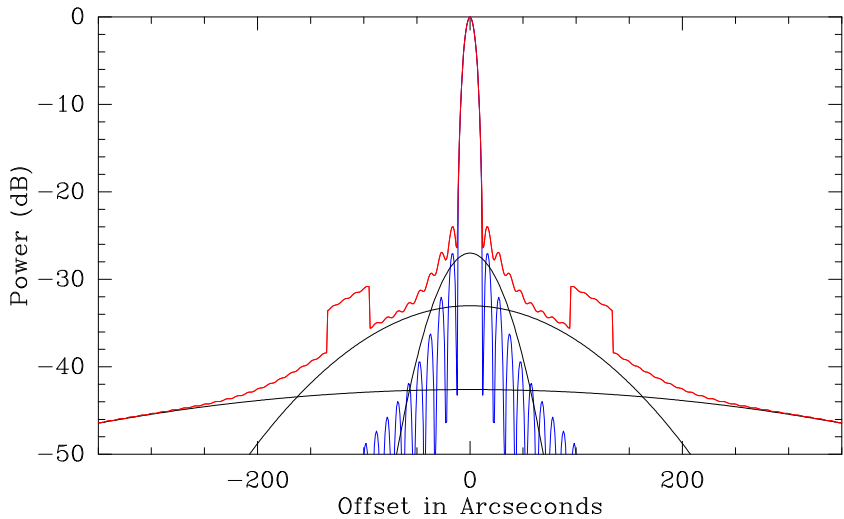


Figure 5: Modelled beam profile at 280 GHz (red), consisting of the diffraction beam with -14 db edge taper (blue), and the three error beams. The effect of the panel buckling is parametrized in a simplified way as an increased beam profile between $95''$ and $135''$ angular offset. The buckling scale factor (2.0 at 280 GHz, cf. Table 1) is derived from fitting the modelled composite profile to the observations. Note that the modelled composite profile at 280 GHz (Fig. 2) has a different shape because the composite profiles are created by differentiating the convolution of the lunar disk with the modelled beam profile shown here. Differentiation is not a deconvolution.

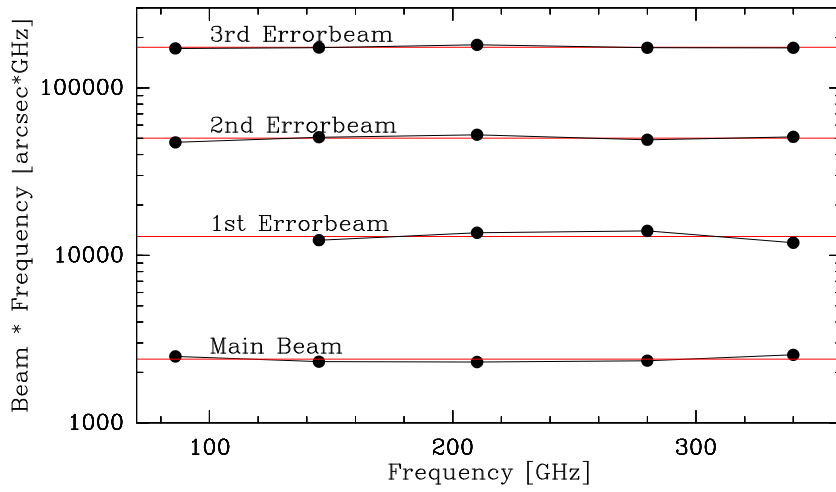


Figure 6: Derived beam widths of the main beam and the three errorbeams multiplied by the observing frequency. Red lines show the average values for the four beams.